

# Searching for ALP Lepton Flavor Violation via ALP Decays at the LHC

Xiaochu Zheng,<sup>1,\*</sup> Ruitian Li,<sup>1</sup> Jing Li,<sup>1</sup> and Hao Sun<sup>1,†</sup>

<sup>1</sup>*Institute of Theoretical Physics, School of Physics, Dalian University of Technology,  
No.2 Linggong Road, Dalian, Liaoning, 116024, People's Republic of China*

In the ALP model, lepton flavor violation (LFV) can arise from off-diagonal ALP–lepton couplings ( $g_{a\ell_i\ell_j}$ ), which are absent in the Standard Model. We focus on ALP production via gluon fusion ( $pp \rightarrow a$ ) at the Large Hadron Collider (LHC), which dominates the ALP mass range of 5–1000 GeV due to its high cross section and manageable backgrounds. We are interested in the decay of an axion into an electron and a muon, two oppositely charged leptons of different flavors. After background suppression, we obtain the sensitivity to ALP in this mass range, finding significantly improved limits for  $5 < m_a < 1000$  GeV, where SM backgrounds are suppressed. Our research is complementary with relevant studies.

## I. INTRODUCTION

Axions are hypothetical particles predicted in extensions of the Standard Model (SM), first introduced by Peccei and Quinn to solve the strong CP problem in quantum chromodynamics (QCD) [1–3]. Axions and axion-like particles (ALP), which generalize the original axion models, are widely predicted in new physics (NP) frameworks like string theory and supersymmetry. Beyond addressing the strong CP problem, they offer solutions to key puzzles: explaining neutrino masses via radiative mechanisms, serving as cold dark matter candidates, and mediating dark matter interactions [4–6].

Testing new fundamental dynamics at a specific energy scale is an effective approach to basic research, and many studies are based on cosmic rays or collider experiments [7–33]. Investigating lepton-flavor-violating (LFV) axions is one of the research directions; scientists search for ALP low-energy cosmic-ray facilities, Supernova, and at colliders [34–39]. Next-generation collider facilities, such as  $\mu$ TRISTAN [31], provide an excellent platform for studying axion-mediated LFV processes. Moreover, existing colliders such as the LHC also play a crucial role in the search for LFV in ALPs.

The aim of our work is to search for LFV in ALP through a process at the LHC. Specifically, we consider the production of an ALP via gluon–gluon fusion, which benefits from a large cross section, followed by its decay into an electron and a muon of opposite charge. After optimizing signal selection and suppressing Standard Model backgrounds, we derive exclusion limits on ALP mass in the range of 5 to 1000 GeV. In this work, we use a center-of-mass energy of  $\sqrt{s} = 14$  TeV and perform analyses un-

der both low-luminosity conditions ( $\mathcal{L} = 300\text{fb}^{-1}$ ) and high-luminosity conditions ( $\mathcal{L} = 3000\text{fb}^{-1}$ ).

In this work, we first describe the theoretical framework of ALP interactions in Section 2, focusing on the effective Lagrangian and key decay kinematics. Section 3 then explores how ALPs are produced in proton–proton collisions, highlighting dominant channels and their modeling. The analysis strategy—including event simulation, selection criteria, and background suppression—is developed in Section 4. In Section 5, we present projected sensitivities to ALP–lepton couplings across several collider configurations. Finally, Section 6 offers a brief summary of our findings and outlook.

## II. THE MODEL

As previously stated, we probe axion LFV properties at the LHC through the decay channel  $a \rightarrow e\mu$ . The axion, being a pseudo-Goldstone boson, exhibits two characteristic interaction features: firstly, it couples to fermion fields through derivative interactions that preserve the global symmetry of the theory; secondly, it interacts with gauge field strengths via a CP-odd coupling, whose unique structure is directly connected to the solution of the strong CP problem. These two fundamental interaction patterns establish the axion’s significant role in extensions of the Standard Model.

The Lagrangian that describes the axion can be expressed as follows [28–30]:

$$\mathcal{L} = \mathcal{L}_f + \mathcal{L}_g + \mathcal{L}_{BB} + \mathcal{L}_{WW} + \mathcal{L}_{e\mu} \quad (1)$$

where:

$$\mathcal{L}_f = -\frac{i\alpha}{f_a} \sum_f g_f m_f^{\text{diag}} \gamma_5 f \gamma^\mu \partial_\mu f \quad (2)$$

\* xiaochuzheng@mail.dlut.edu.cn

† haosun@dlut.edu.cn

$$\mathcal{L}_g = -C_g \frac{a}{f_a} G_{\mu\nu}^A \tilde{G}^{\mu\nu,A} \quad (3)$$

$$\mathcal{L}_{BB} = -C_{BB} \frac{a}{f_a} B_\mu^i \tilde{B}^{\mu,i} \quad (4)$$

$$\mathcal{L}_{WW} = -C_{WW} \frac{a}{f_a} W_{\mu\nu}^i \tilde{W}^{\mu\nu,i}, \quad (5)$$

where  $i = 1, 2, 3$  represents the gage indices SU(2) and  $A = 1, \dots, 8$  denotes the color indices SU(3), with  $W_{\mu\nu}^i$  and  $B_{\mu\nu}^i$  being the corresponding dual field strength tensors. The ALP field and its decay constant are denoted by  $a$  and  $f_a$ , respectively. The axion-ALP coupling is described by the Lagrangian  $\mathcal{L}_f$ , where all coefficients in  $\mathcal{L}_f$  are set to zero in our work. Firstly, we express the axion-gluon coupling coefficient as:

$$g_{agg} = \frac{C_g}{f_a} \quad (6)$$

After transforming  $W_{\mu\nu}^i$  and  $B_{\mu\nu}^i$  into the physical fields  $\gamma$ ,  $Z$ , and  $W^\pm$ , the part of Eq. 1 that does not involve LFV can be expressed as:

$$\begin{aligned} \mathcal{L} = & -\frac{ia}{f_a} \sum_f g_{af} m_f^{\text{diag}} \bar{f} \gamma_5 f - C_g \frac{a}{f_a} G_\mu^A \tilde{G}^{\mu\nu A} \\ & - \frac{a}{f_a} \left[ (C_{BB} c_w^2 + C_{WW} s_w^2) F_{\mu\nu} \tilde{F}^{\mu\nu} \right. \\ & + (C_{BB} s_w^2 + C_{WW} c_w^2) Z_{\mu\nu} \tilde{Z}^{\mu\nu} \\ & + 2(C_{WW} - C_{BB}) c_w s_w F_{\mu\nu} \tilde{Z}^{\mu\nu} \\ & \left. + C_{WW} W_{\mu\nu}^+ \tilde{W}^{\mu\nu-} \right]. \quad (7) \end{aligned}$$

Where  $F_{\mu\nu}$ ,  $W_{\mu\nu}$  and  $Z_{\mu\nu}$  are the field strength tensors of the photon,  $W^\pm$ , and  $Z$  bosons respectively. Moreover, the dimensionful couplings of the photon and electroweak bosons to the ALP can be represented by  $C_{WW}$  and  $C_{BB}$ . Similarly as the axion-gluon coupling coefficient, we set other coupling coefficients as :

$$g_{a\gamma\gamma} = \frac{4}{f_a} (C_{BB} C_W^2 + C_{WW} S_W^2), \quad (8)$$

$$g_{a\omega\omega} = \frac{4}{f_a} C_{WW}, \quad (9)$$

$$g_{aZZ} = \frac{4}{f_a} (C_{BB} S_W^2 + C_{WW} C_W^2), \quad (10)$$

$$g_{a\gamma Z} = \frac{8}{f_a} S_W C_W (C_{WW} - C_{BB}). \quad (11)$$

Where  $C_W$  and  $S_W$  are the cosine and sine of the Weinberg angle respectively, characterizing the rotation between the electroweak fields and the physical fields, as shown in:

$$\begin{pmatrix} W_\mu^3 \\ B_\mu \end{pmatrix} = \begin{pmatrix} c_W & s_W \\ -s_W & c_W \end{pmatrix} \begin{pmatrix} Z_\mu \\ A_\mu \end{pmatrix}, \quad (12)$$

Especially, the interactions of the vector lepton current and the axial-vector lepton current for the LFV couplings of axion-like particles are described by the following Lagrangian[39, 40], where the electron and muon are mass eigenstates:

$$\mathcal{L}_{e\mu} = \frac{\partial_\mu a}{f_a} \bar{e} \gamma^\mu (C_{e\mu}^V + C_{e\mu}^A \gamma_5) \mu, \quad (13)$$

The dimensionless coefficients  $C_{e\mu}^{AV}$  form Hermitian matrices in flavor space, satisfying the relation  $C_{e\mu}^{VA*} = C_{e\mu}^{AV}$ . In our work, we treat  $C_{e\mu}^{AV}$  as a free parameter to be scanned over, which maintains the generality of the theory while providing flexibility for experimental detection. To simplify the analysis, we define dimensionless scalar/pseudoscalar coupling coefficients  $g_{S,P}$  from this expression, which will be used in subsequent physical process calculations.

$$g_{e\mu}^V = \frac{C_{e\mu}^V (m_\mu - m_e)}{2f_a}, \quad (14)$$

$$g_{e\mu}^A = \frac{C_{e\mu}^A (m_\mu - m_e)}{2f_a}, \quad (15)$$

Since the muon mass is much larger than the electron mass ( $m_\mu \gg m_e$ ), the above formula can be simplified to the following form:

$$g_{e\mu}^V = \frac{C_{e\mu}^V m_\mu}{2f_a}, \quad (16)$$

$$g_{e\mu}^A = \frac{C_{e\mu}^A m_\mu}{2f_a}, \quad (17)$$

This approximation preserves the dominant physical effects while significantly reducing computational complexity.

We treat the ALP mass  $m_a$  as a free parameter and probe LFV in ALP through the decay channel  $a \rightarrow e^\pm \mu^\mp$ . In the following analysis, we assume the equality of vector and axial-vector couplings ( $g_{e\mu}^V = g_{e\mu}^A$ ), which reduces the parameter space dimensionality while preserving the essential physics.

Its decay width is [24]:

$$\begin{aligned} \Gamma(a \rightarrow e\mu) = & \frac{m_a}{8\pi} \sqrt{\left(1 - \frac{(m_\mu + m_e)^2}{m_a^2}\right) \left(1 - \frac{(m_\mu - m_e)^2}{m_a^2}\right)} \\ & \times \left[ |g_{e\mu}^V|^2 \left(1 - \frac{(m_\mu + m_e)^2}{m_a^2}\right) \right. \\ & \left. + |g_{e\mu}^A|^2 \left(1 - \frac{(m_\mu - m_e)^2}{m_a^2}\right) \right] \quad (18) \end{aligned}$$

For  $m_a \gg m_\mu + m_e$ , this decay width corresponds to the following ALP proper decay length:

$$\begin{aligned}
\tau(a \rightarrow e\mu) &\approx 16\pi \frac{1}{m_a^3 (|g_{e\mu}^V|^2 + |g_{e\mu}^A|^2)} \\
&\approx 10^{-6} \text{ ms} \left( \frac{m_a}{1 \text{ GeV}} \right)^{-3} \\
&\quad \times \left( \frac{10^{-8}}{|g_{e\mu}^V|^2 + |g_{e\mu}^A|^2} \right)^2
\end{aligned} \tag{19}$$

Regarding the coupling  $g_{e\mu}^{AV}$ , the experimental bounds for the investigated mass range are currently between  $10^{-2}$  and  $10^{-4}$  [41]. Related studies provide even tighter constraints within the corresponding mass window, reaching the level of  $10^{-4}$  to  $10^{-5}$ .

### III. THE COLLISION PROCESS TAKES PLACE AT THE LHC

In this section, we investigate several processes involving LFV ALPs, including the production of axion-like particles and their decay into electron-muon pairs. Our analysis covers the axion mass range  $m_a = 5 - 1000 \text{ GeV}$  of particular relevance for current collider experiments. To implement our LFV ALP model in collider simulations, we first use FeynRules [42, 43] to convert the Lagrangian into a machine-readable model file. This file encodes all interaction terms (including fermion and gauge couplings), providing the theoretical input for subsequent Monte Carlo simulations. The model is then imported into MadGraph5.aMC@NLO framework [44, 45], where we specify the signal processes and calculate the leading-order (LO) cross sections as functions of the ALP mass  $m_a$  and the coupling constant  $g_{e\mu}^{AV}$ . These calculations provide theoretical benchmark expectations for future analyses. In Section 3.1, we identify the most favorable ALP production mechanism at the LHC through cross section comparisons of key channels (e.g., the gluon fusion process  $gg \rightarrow a$ ). Section 3.2 subsequently presents systematic calculations of ALP branching ratios, with a particular focus on the competition between the lepton-flavor-violating channel  $a \rightarrow e\mu$  and the dominant decay modes (for example,  $a \rightarrow \gamma\gamma$ ). These results establish the theoretical foundation for experimental sensitivity estimates.

#### A. process selection

There are three types of collision processes that produce axions. In our calculation, the coupling parameters were chosen with reference to those used in previous studies [32, 33]. These processes are:

Case 1. Axion production through coupling with quarks.

Case 2. Axion production through coupling with  $V$  bosons, including  $pp \rightarrow Z+a$  and  $pp \rightarrow W \pm +a$ .

Case 3. Axion production via coupling to gluons.

Among the production mechanisms, We observe that quark-fusion contributions to axion production are strongly suppressed relative to gluon fusion. This suppression originates from the large effective gluon coupling  $c_{\text{eff}}^G = c_u + c_d + c_s \approx 3$  and the fact that the squared matrix element for gluon fusion scales as  $|\mathcal{M}_g|^2 \propto m_a^3$ , while for quark fusion it scales as  $|\mathcal{M}_q|^2 \propto m_a m_q^2$  with  $m_q \ll m_a$ . Consequently, the quark channel is subdominant. For this reason, we restrict our analysis to axions with  $m_a > 5 \text{ GeV}$  [46]. This exclusion ensures the reliability of the parameters used in subsequent analyses.

For the other processes, we compute the cross sections within MadGraph5.aMC@NLO [44, 45], using the most recent values of the coupling coefficients reported in the literature. Representative mass benchmarks are selected and summarized in Table 1. Our parameter choices follow standard conventions adopted in related studies. The LFV couplings  $g_{e\mu}^{AV}$  are varied over a range of benchmark values that balance theoretical plausibility with numerical feasibility, enabling a systematic assessment of experimental sensitivity.

Because the cross section of Case 3 is larger and the background is cleaner,  $gg \rightarrow a \rightarrow e \pm \mu \mp$  is chosen as the research process. Its Feynman diagram is represented in Figure 1. We then calculate the decay branching ratios of the axion.

The signal cross section is given by the production cross section multiplied by the branching ratio for decays into an electron-muon pair, as given in Eq.20. This relation fully characterizes the complete physical process chain from ALP production to LFV decays.

$$\sigma_{\text{total}} = \sigma_{\text{process}} \times \text{BR}(a \rightarrow e \pm \mu \mp) \tag{20}$$

#### B. Decay width

The main decay channels of the ALP are diphoton decay ( $a \rightarrow \gamma\gamma$ ) and digluon decay ( $a \rightarrow gg$ ), where the theoretical calculation of its decay width must incorporate the effects of the corresponding coupling coefficients  $g_{a\gamma\gamma}$  and  $g_{agg}$  in which we have referred to these studies on coupling coefficients [32, 33]. Additionally, when the ALP mass exceeds approximately 350 GeV (about

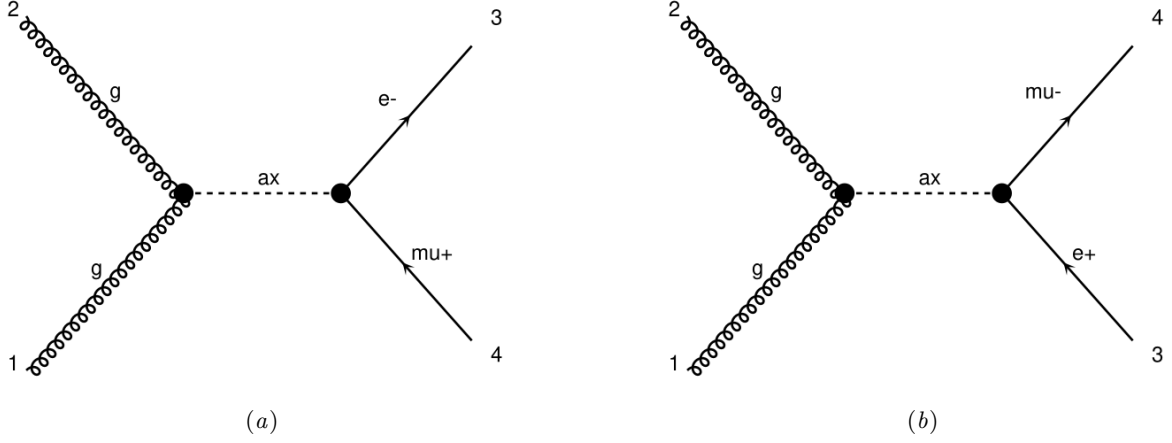


FIG. 1: In high-energy collisions at the Large Hadron Collider (LHC), axion-like particles (ALPs)—denoted as "ax" in the diagram—are produced via gluon–gluon fusion, where gluons are the force carriers of the strong interaction. The left panel shows the ALP decaying into  $e^-\mu^+$ , while the right panel depicts its decay into  $e^+\mu^-$ . As charged leptons with relatively low mass, electrons and muons provide clean experimental signatures in particle detectors, enabling precision studies of non-perturbative QCD effects and the confinement mechanism.

TABLE I: Production cross sections calculated in MadGraph at  $\sqrt{s} = 14\text{TeV}$  with parameter settings  $f_a = 1000\text{GeV}$ ,  $C_g = C_Z = C_W = 0.025$  demonstrate the detectability features of this theoretical model under LHC conditions. These parameter choices align with current theoretical expectations while enabling experimental comparisons.

$m_a$ (GeV)	$\sigma(pp \rightarrow Za)$ (pb)	$\sigma(pp \rightarrow W^\pm a)$ (pb)	$\sigma(gg \rightarrow a)$ (pb)
5	0.003	0.01	1021
50	0.002	0.006	248.5
100	0.0013	0.0035	95.03
200	0.00059	0.0015	28.82
500	0.00011	0.00029	3.845
1000	1.73e-5	4.5e-5	0.53

twice the top quark mass), the decay channel ALP to  $t\bar{t}$  which is on-shell must also be taken into account[33]. These coupling parameters directly determine the relative branching ratios between different decay channels. Therefore, the decay branching ratios are given by Eq. 21 and Eq. 22, where  $\Gamma_{a \rightarrow \gamma\gamma}$  denotes the decay width of the ALP into two photons and  $\Gamma_{a \rightarrow gg}$  represents the decay width in two gluons. The relative magnitude of these decay channels directly reflects the difference in coupling strengths between the ALP and the gauge fields.

Taking into account the contribution of the lepton-flavor-violating decay channel  $\Gamma_{a \rightarrow e\pm\mu\mp}$ , the total decay

branching ratio can be fully described by Eq. 21. This expression incorporates the competition mechanism between gauge boson final states and LFV final state.

$$\text{BR}(a \rightarrow e \pm \mu \mp) = \frac{\Gamma_{a \rightarrow e\pm\mu\mp}}{\Gamma_{a \rightarrow e\pm\mu\mp} + \Gamma_{a \rightarrow gg} + \Gamma_{a \rightarrow \gamma\gamma}} \quad (21)$$

$$\text{BR}(a \rightarrow e \pm \mu \mp) = \frac{\Gamma_{a \rightarrow e\pm\mu\mp}}{\Gamma_{a \rightarrow e\pm\mu\mp} + \Gamma_{a \rightarrow gg} + \Gamma_{a \rightarrow \gamma\gamma} + \Gamma_{a \rightarrow t\bar{t}}} \quad (22)$$

Here, the partial decay widths for the LFV channel  $\Gamma_{a \rightarrow e\pm\mu\mp}$ , the digluon decay width  $\Gamma_{a \rightarrow gg}$ , the decay width  $\Gamma_{a \rightarrow \gamma\gamma}$  and the decay width  $\Gamma_{a \rightarrow t\bar{t}}$  are given by

Eq. 23, Eq. 24 , Eq. 25 and Eq. 27 respectively. These expressions fully characterize the dominant decay properties of ALP within the Standard Model particle spectrum. They are :

$$\Gamma_{a \rightarrow e\mu} = \frac{m_a (|g_{e\mu}|^2 + |g_{\mu e}|^2)}{4\pi}, \quad (23)$$

$$\Gamma_{a \rightarrow gg} = \frac{2m_a^3 g_{agg}^2}{\pi}, \quad (24)$$

$$\Gamma_{a \rightarrow \gamma\gamma} = \frac{m_a^3 g_{a\gamma\gamma}^2}{4\pi}, \quad (25)$$

$$(26)$$

$$\Gamma(a \rightarrow t\bar{t}) = \frac{3m_a m_t^2 |g_t^{\text{eff}}|^2}{8\pi} \sqrt{1 - \frac{4m_t^2}{m_a^2}}. \quad (27)$$

#### IV. EXPERIMENTAL SETUP AND SIMULATION

This section details the calculation methods and detector configurations used to suppress various Standard Model background signals. We present the expected event rates at  $\sqrt{s} = 14\text{TeV}$  center-of-mass energy, for both ( $\mathcal{L} = 300\text{fb}^{-1}$ ) (current operation) and ( $\mathcal{L} = 3000\text{fb}^{-1}$ ) (HL-LHC upgrade) integrated luminosity scenarios. These calculations provide critical inputs for subsequent sensitivity analyses.

##### A. Signal and relevant SM background processes

We perform Monte Carlo simulations for signal and relevant Standard Model (SM) background processes using MadGraph5.aMC@NLO, with signal implementation via UFO model files in the ALP EFT framework. All calculations are strictly limited to leading-order (LO) accuracy without including next-to-leading order (NLO) or higher corrections. Following LO matrix element generation, Pythia 8 [47] is employed to simulate parton shower processes while explicitly disabling higher-order QCD options to maintain consistency with LO matrix elements. After conducting signal-to-background analysis at the parton level and approximating detector effects through momentum smearing, the LHE output files from MadGraph5.aMC@NLO are processed by the Python-based tool Pylhe for further analysis. Next, Delphes3 is used to simulate the detector effects based on the default detector configuration card for the LHC [48]. This end-to-end workflow ensures consistency from theoretical simulation

to experimental observation while balancing computational efficiency with the current theoretical uncertainty level of the ALP EFT framework through strict LO precision control.

We consider five quark flavors (u, c, s, d, b). This work focuses on ALPs in the mass range of 5–1000 GeV. For simulations, we assign the following benchmark values to the model parameters: collision energy  $\sqrt{s} = 14\text{TeV}$ , axion decay constant  $f_a = 1000\text{GeV}$ , coupling coefficients  $g_{agg} = g_{a\gamma\gamma} = 2.5 \times 10^{-5}$ , and set temporarily lepton-flavor-violating couplings  $g_{e\mu}^A = g_{e\mu}^V = 5 \times 10^{-5}$ . Following previous studies [32, 33] and considering that the flavor-conserving axion-fermion couplings are proportional to fermion masses (with negligible contributions), we set  $g_f = 0$ . This parameter choice not only covers the main detection energy range of the LHC but also significantly reduces the theoretical computation complexity.

The process is  $g g \rightarrow a$ , with  $a \rightarrow e^\pm \mu^\mp$ , where the final state consists of an electron and a muon. Therefore, we consider these main backgrounds. They include backgrounds with the same final state and backgrounds caused by detector errors that lead to the identification of the same final state. The signal process is  $g g \rightarrow a$ , followed by  $a \rightarrow e^\pm \mu^\mp$ , yielding a final state consisting of an electron and a muon. Therefore, we consider the following main backgrounds: those that produce the same final state at the generator level, as well as those arising from detector misidentification or reconstruction errors that mimic this signature.

We referred to the ATLAS study on the "e,mu" final state and considered the following background processes [49]: (1) TOP-quark backgrounds :Proton–proton collisions produce a top–antitop  $t\bar{t}$  pair, which subsequently decays into  $W + W - b\bar{b}$ . The W+W- bosons then undergo leptonic decays, yielding an electron and a muon with opposite electric charges and the corresponding neutrinos. (2) In addition, there is a background contribution from tW associated production, where the electron and muon originate separately from the decays of the top quark (t) and the W boson, respectively. (3) Backgrounds also arise from the leptonic decays of Z and W bosons. (4) Backgrounds also include misidentification by the detector. These backgrounds primarily arise from the misidentification of the number of jets. Based on these similar final states, we consider six Standard Model background processes. Taking both accuracy and computational cost into account, we generated the following simulated events for these six background processes. The background processes considered in this analysis are:

BG1: The pair production of top–antitop quarks ( $pp \rightarrow t\bar{t}$ ) proceeds via two distinct decay channels:

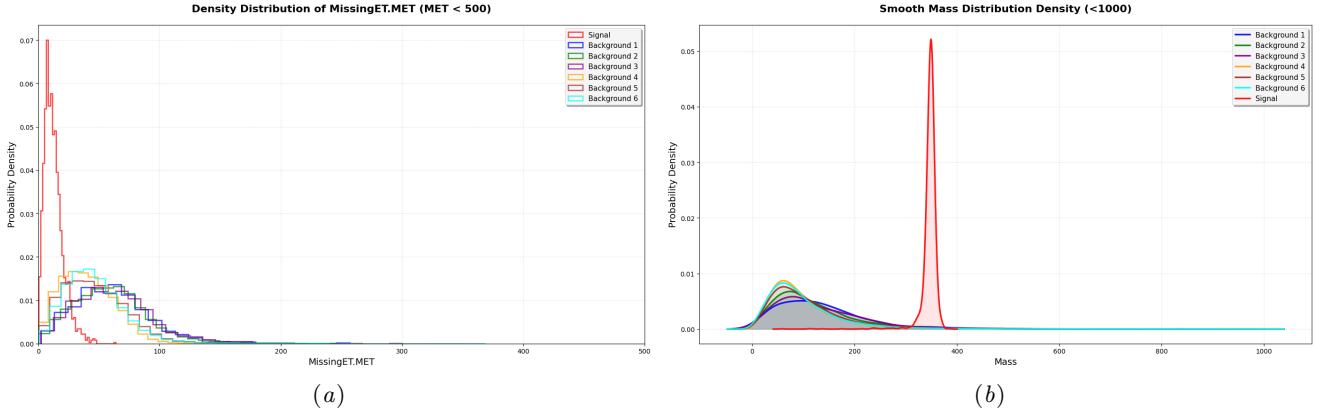


FIG. 2: The distributions in Fig.2 clearly characterize the event topology for different observables, where signal and background components are distinguished by the legend in the upper-right panel. Specifically: (a) shows the missing transverse energy ( $E_T^{\text{miss}}$ ) distribution. Signal events (red) exhibit a pronounced tail at high  $E_T^{\text{miss}}$ , arising from the undetected axion-like particle (ALP) in the process  $pp \rightarrow a \rightarrow e^\pm \mu^\mp + E_T^{\text{miss}}$ . In contrast, background events (blue) cluster predominantly at low  $E_T^{\text{miss}}$ , primarily due to instrumental effects and measurement uncertainties; (b) presents the  $m_{e\mu}$  (electron-muon invariant mass) spectrum, with signal events peaking sharply near the axion mass  $m_a$  (dashed line) from resonant  $a \rightarrow e\mu$  decays, contrasted with the smooth continuum distribution of backgrounds. These distinctive features enable effective kinematic separation through optimized selection cuts.

(i)  $pp \rightarrow t\bar{t} \rightarrow W + W - b\bar{b} \rightarrow e^- \mu^+ \nu_e \bar{\nu}_\mu b\bar{b}$ , (ii)  $pp \rightarrow t\bar{t} \rightarrow W + W - b\bar{b} \rightarrow e^+ \mu^- \bar{\nu}_e \nu_\mu b\bar{b}$ . Both processes have an identical leading-order cross section of 6731 fb. For each channel, we generated 500,000 Monte Carlo events.

BG2: Single top quark production in association with a  $W$  boson gives rise to four distinct charge and flavor configurations: (i)  $pp \rightarrow tW^- \rightarrow e^- \mu^+ \nu_e \bar{\nu}_\mu b$ , (ii)  $pp \rightarrow tW^- \rightarrow e^+ \mu^- \bar{\nu}_e \nu_\mu \bar{b}$ , (iii)  $pp \rightarrow \bar{t}W^+ \rightarrow e^- \mu^+ \nu_e \bar{\nu}_\mu \bar{b}$ , (iiii)  $pp \rightarrow \bar{t}W^+ \rightarrow e^+ \mu^- \bar{\nu}_e \nu_\mu b$ . Each of these four processes has an identical cross section of 377.8 fb. We generated 500,000 Monte Carlo events for each individual channel.

BG3: Single top quark production in association with an additional jet ( $tW + \text{jet}$ ) must also be taken into account. We consider four distinct processes: (i)  $pp \rightarrow tW \rightarrow e^- \mu^+ \nu_e \bar{\nu}_\mu b j$ , (ii)  $pp \rightarrow tW \rightarrow e^+ \mu^- \bar{\nu}_e \nu_\mu \bar{b} j$ , (iii)  $pp \rightarrow \bar{t}W^+ \rightarrow e^- \mu^+ \nu_e \bar{\nu}_\mu \bar{b} j$ , (iiii)  $pp \rightarrow \bar{t}W^+ \rightarrow e^+ \mu^- \bar{\nu}_e \nu_\mu \bar{b} j$ . Each of these four processes has a cross section of 688.7 fb, and we generated 500,000 events for each process.

BG4: As a direct source of  $e\mu$  final states, we consider  $W^+W^-$  production, which proceeds via two charge-conjugate channels: (i)  $pp \rightarrow W + W^- \rightarrow e^- \mu^+ \nu_e \bar{\nu}_\mu$ , (ii)  $pp \rightarrow W + W^- \rightarrow e^+ \mu^- \bar{\nu}_e \nu_\mu$ . Due to the relatively high efficiency of selecting events with exactly one electron and one muon, both channels are significant backgrounds. Each process has a cross section of 851.3 fb, and we generated 250,000 events for each channel.

BG5: As a source of  $e\mu$  final states accompanied by a jet, we consider  $W+W^-$  production in association with an additional jet ( $W+W^-j$ ). This process includes two charge-conjugate configurations: (i)  $pp \rightarrow W + W^- \rightarrow e^- \mu^+ \nu_e \bar{\nu}_\mu j$ , (ii)  $pp \rightarrow W + W^- \rightarrow e^+ \mu^- \bar{\nu}_e \nu_\mu j$ . Both channels have a cross section of 1277 fb, and we generated 500,000 events for each configuration.

BG6: The  $ZW$  associated production background must also be considered. We simulate the  $pp$  to  $ZW$  process (where the  $W$  can be either  $W^+$  or  $W^-$ ), which yields a three-lepton final state. Due to lepton misidentification in the detector—such as one lepton being missed or misreconstructed—this three-lepton signature can be misidentified as an  $e\mu$  final state. Specifically, we generate events for  $pp$  to  $pp \rightarrow WZ \rightarrow lll$  (the three leptons include either a pair of electrons with opposite charges or a pair of muons with opposite charges). For this  $ZW$  background process, we generated 500,000 events.

To estimate the sensitivity reach of the ALP coupling strength  $g_{ALP}$ , we perform a detailed evaluation of both signal and background event yields at the LHC's design center-of-mass energy of  $\sqrt{s} = 14\text{TeV}$ . The total expected event count  $N_{total}$  is defined as:

$$N_{s,b} = \sigma_{s,b} \times \mathcal{L} \times \eta_{s,b} \quad (28)$$

Here,  $\mathcal{L}$  represents the integrated luminosity, with the scenarios  $\mathcal{L} = 300\text{fb}^{-1}$  (low luminosity) and  $\mathcal{L} =$

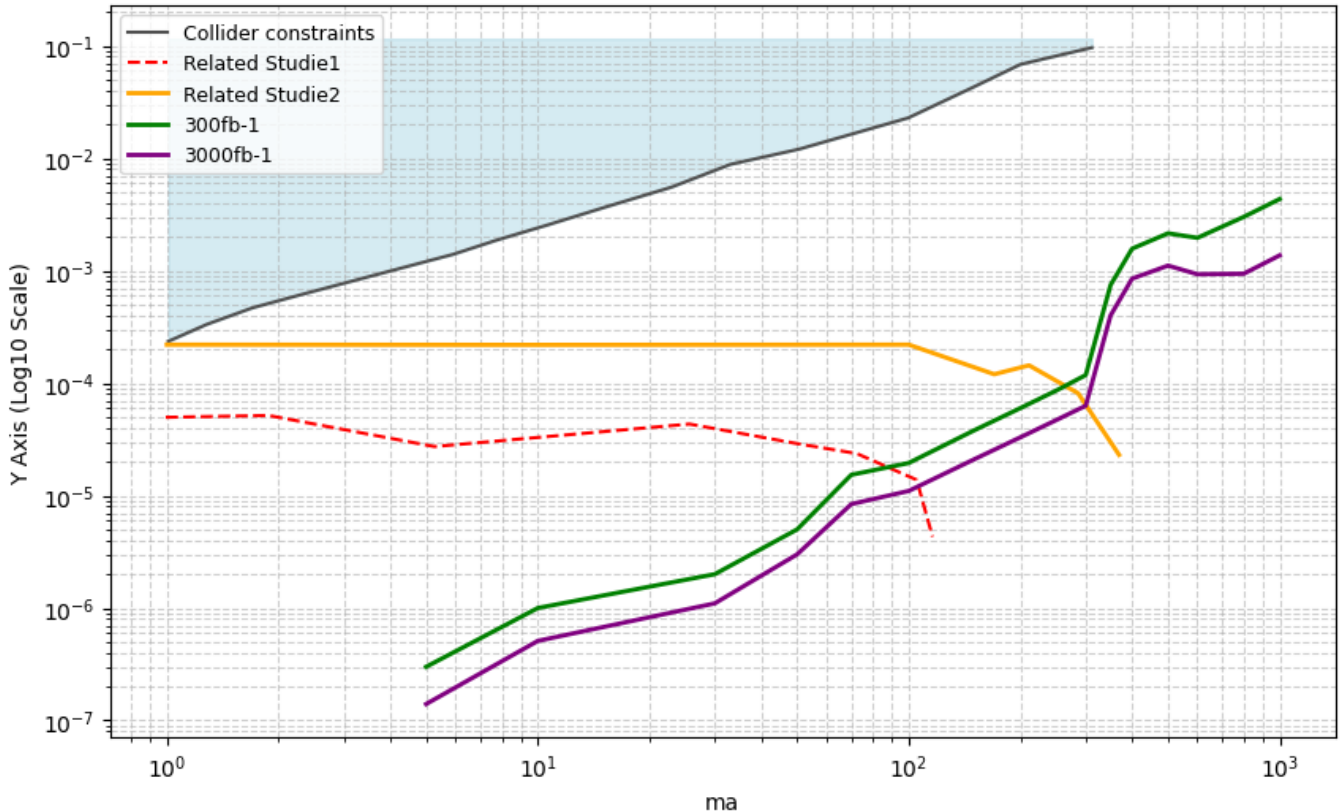


FIG. 3: In this paper, the derived exclusion limits are compared with the most stringent experimental constraints from dilepton final states, specifically the  $Mu - \bar{M}u$  experiment. Related theoretical studies predicting axion production cross sections in this mass range are referenced to provide context for the experimental constraints. The kinematic distributions used in this analysis differ from those employed in previous collider searches, offering complementary sensitivity to axion-like particle production.

$3000 \text{ fb}^{-1}$  (high luminosity). The selection efficiency  $\eta = N_{\text{selected}}/N_{\text{sim}}$  quantifies the fraction of simulated events passing the selection criteria, where  $N_{\text{selected}}$  ( $N_{\text{sim}}$ ) denotes the number of selected (simulated) events. The significance formula is given by:

$$Z = \frac{N_s}{\sqrt{N_s + N_b}} \quad (29)$$

### B. Event selection

We propose to search for ALPs in the mass range 5–1000 GeV, with  $m_a = 350 \text{ GeV}$  serving as our benchmark scenario to illustrate the analysis procedure. As demonstrated in Fig. 2, we have identified two optimal discriminants for signal-background separation: (i) the missing transverse energy  $E_T$ , which exhibits significant differences between signal and background processes due to the invisible decays of the W bosons, and (ii) the  $e\mu$  invariant mass  $m_{e\mu}$ , which peaks

sharply near the axion mass for signal events. In Fig. 2, each data series is distinguished by a specific color as indicated in the legend: the Signal is shown in red, Background 1 in blue, Background 2 in green, Background 3 in purple, Background 4 in yellow, Background 5 in brown, and Background 6 in cyan—allowing for clear visual identification of each component within the plot. After systematically evaluating other potential observables including angular correlations and transverse momentum balances, we find that the combined cuts on these two particular variables provide the most effective background suppression while maintaining maximal signal efficiency. We apply optimized selection cuts on both observables to maximize the signal significance  $\mathcal{Z} = N_S/\sqrt{N_S + N_B}$ .

Given that the leptonic final states in background events predominantly originate from  $W^\pm$  boson decays ( $W^\pm \rightarrow \ell^\pm \nu$ ), which produce genuine missing transverse energy from neutrinos, we impose a stringent upper cut of  $E_T^{\text{miss}} < 20 \text{ GeV}$  to suppress this background compo-

TABLE II: The signal entry and each background entry in the header represent the number of events generated after selection cuts. The first column lists the axion mass values. The second column shows the corresponding number of signal events surviving the selection criteria. Columns three through eight display the numbers of background events from six distinct sources. The ninth column gives the axion production cross section ( $\sigma_a$ ), while the tenth and eleventh columns present the minimum detectable cross sections under low- and high-luminosity conditions ( $\sigma_{\min}^{\text{low}}$  and  $\sigma_{\min}^{\text{high}}$ ), respectively. As clarified in the table caption and footnotes,  $\sqrt{s}$  denotes the center-of-mass energy,  $f_a$  is the axion decay constant,  $\sigma_a$  represents the production cross section, and  $\sigma_{\min}^{\text{low/high}}$  indicate the expected sensitivity limits for the respective luminosity scenarios.

$M_a$	Sig ( $2 \times 10^4$ )	Background Events						gg→a Cross Section (fb)	Min. Detectable Cross Section and Upper Limit	
		B1	B2	B3	B4	B5	B6		$\mathcal{L} = 300 \text{ fb}^{-1}$	$\mathcal{L} = 3000 \text{ fb}^{-1}$
		$10^6$	$2 \times 10^6$	$2 \times 10^6$	$5 \times 10^5$	$10^6$	$5 \times 10^5$		$\sigma, \text{ UL} \times 10^{-4}$	$\sigma, \text{ UL} \times 10^{-4}$
1000	1191	0	0	0	0	0	0	533.4	0.22 (43.4)	0.11 (13.7)
800	1415	0	0	0	0	0	0	1064	0.23 (30.1)	0.054 (9.4)
600	1705	0	0	0	2	0	0	2388	0.24 (19.6)	0.055 (9.3)
500	1278	0	0	0	5	2	0	3832	0.54 (21.5)	0.14 (11.1)
400	1729	1	10	1	53	69	16	6593	0.71 (15.7)	0.21 (8.5)
350	1692	0	19	1	87	27	12	8966	0.70 (7.46)	0.20 (4.0)
300	1807	2	22	2	175	34	36	12640	0.70 (1.18)	0.20 (0.63)
250	2128	5	28	2	175	34	36	18470	0.77 (0.86)	0.23 (0.47)
200	2161	2	59	7	277	50	85	28740	0.92 (0.6)	0.28 (0.33)
150	2213	4	69	4	516	88	65	48660	1.16 (0.38)	0.35 (0.21)
100	2116	6	61	6	617	72	57	94790	1.29 (0.195)	0.39 (0.11)
70	1475	3	14	0	316	32	30	159720	1.34 (0.153)	0.40 (0.084)
50	2152	2	31	1	388	52	44	247800	1.02 (0.05)	0.31 (0.03)
30	1620	1	3	0	69	17	16	636800	0.66 (0.02)	0.19 (0.011)
10	135	0	1	1	9	1	3	939803	3.0 (0.01)	0.86 (0.0051)
5	165	0	0	0	1	0	0	1021630	1.8 (0.003)	0.28 (0.0014)

ment. The  $e^\pm\mu^\mp$  pairs from signal events exhibit a concentrated distribution since they originate from resonant axion decays ( $a \rightarrow e^\pm\mu^\mp$  with  $\mathcal{B}(a \rightarrow \ell\ell) \sim 10^{-3}$ ), whereas background dileptons from electroweak boson decays ( $W^+W^- \rightarrow \ell\nu\ell\nu$ ) show broader kinematic distributions due to uncorrelated production mechanisms. This distinctive behavior is quantitatively demonstrated in Fig. 2. To enhance the signal-to-background ratio, we select events within the mass window  $320 \text{ GeV} < m_{e\mu} < 360 \text{ GeV}$ .

## V. RESULT

After applying the selection cuts in parallel, the results are summarized in Table 2. The table presents the final

event yields for both signal ( $N_S$ ) and background ( $N_B$ ) processes across different axion mass hypotheses. The minimum detectable cross section  $\sigma_{\min}$  is calculated using Eq. 28 and Eq. 29 for an exclusion sensitivity corresponding to a significance of  $Z = 2$  (approximately 95% CL), where  $\epsilon$  denotes the combined selection efficiency. Additionally, the upper limits on the coupling strength  $g_{e\mu}^{A,V}$  are derived from Eq. 20 under both the Run 3 luminosity scenario ( $\mathcal{L} = 300 \text{ fb}^{-1}$ ) and the HL-LHC projection ( $\mathcal{L} = 3000 \text{ fb}^{-1}$ ).

Figure 3 presents the upper limits on the coupling coefficients derived from our analysis at integrated luminosities of  $L = 300 \text{ fb}^{-1}$  (green curve) and  $L = 3000 \text{ fb}^{-1}$  (purple curve). The blue shaded region indicates existing experimental constraints from references [41, 50], which are particularly relevant for the axion mass range

investigated in our work. The red dashed line shows the exclusion limit from the reference study under the  $\sqrt{s} = 110$  GeV scenario, while the orange solid line represents the exclusion limit from the reference study under the  $\sqrt{s} = 346$  GeV scenario [31]. Our findings demonstrate that lower axion masses correspond to: (1) higher branching ratios for lepton flavor violating (LFV) decays, and (2) larger production cross sections, both of which significantly enhance the experimental sensitivity. In particular, compared to the study in  $\sqrt{s} = 110$  GeV, our analysis yields tighter constraints on the ALP coupling for  $m_a$  masses in the range of 5–110 GeV. Compared to the study in  $\sqrt{s} = 346$  GeV, our work provides even stronger limits over an extended mass range of 5–300 GeV. Additionally, we have also computed exclusion limits for  $m_a$  from 350 GeV to 1000 GeV. However, due to the two aforementioned factors—namely, the opening of the  $t\bar{t}$  decay channel above 350 GeV and the reduced signal sensitivity at high masses—our analysis is unable to set stringent constraints in this high-mass region.

## VI. CONCLUSIONS

In this work, we systematically investigated the sensitivity potential of the LHC for both its current operational phase and the planned high-luminosity upgrade, corresponding to integrated luminosities of  $L = 300 \text{ fb}^{-1}$  and  $L = 3000 \text{ fb}^{-1}$  respectively, at a center-of-mass energy of  $\sqrt{s} = 14 \text{ TeV}$ . Building upon established theo-

retical frameworks, we adopted benchmark coupling coefficients from previous studies and conducted detailed probes of the LFV coupling coefficients  $g_{e\mu}^{A,V}$  through the distinctive gluon fusion process  $gg \rightarrow a(e^\pm\mu^\mp)$ , where  $a$  represents ALP. This channel provides exceptional sensitivity to new physics due to its clean final-state signature and suppressed Standard Model background contributions.

Our analysis incorporates findings from recent studies on the phenomenology of ALP. After evaluating the characteristic decay modes of axion-like particles, we established a conservative parameter space guided by the most stringent existing constraints. Then these parameters were implemented in a complete simulation framework, including event generation, parton shower modeling, and detector response simulation. The validity of our parameter choices was confirmed through systematic consistency checks between simulated observables and theoretical expectations.

In summary, we have considered a novel production and decay process and computed the sensitivity of the LHC to the lepton flavor violating coupling coefficient  $g_{e\mu}^{A,V}$  of ALPs over a mass range from 5 GeV to 1000 GeV based on this channel. Our analysis demonstrates that, compared to previous approaches, our method achieves superior sensitivity in specific mass regions—namely 5–100 GeV and 110–300 GeV—while also exhibiting strong complementarity with existing strategies across the entire mass spectrum.

- 
- [1] R. D. Peccei and H. R. Quinn, *Physical Review Letters* **38**, 1440 (1977).
  - [2] F. Wilczek, *Physical Review Letters* **40**, 279 (1978).
  - [3] S. Weinberg, *Physical Review Letters* **40**, 223 (1978).
  - [4] J. Preskill, M. B. Wise, and F. Wilczek, *Physics Letters B* **120**, 127 (1983).
  - [5] L. Abbott and P. Sikivie, *Physics Letters B* **120**, 133 (1983).
  - [6] M. Dine and W. Fischler, *Physics Letters B* **120**, 137 (1983).
  - [7] T. Han, T. Li, and X. Wang, in *Snowmass 2021* (2022) arXiv:2203.05484 [hep-ph].
  - [8] C.-X. Yue, S. Yang, H. Wang, and N. Zhang, *Physical Review D* **105**, 115027 (2022), arXiv:2204.04702 [hep-ph].
  - [9] J. Liu, X. Ma, L.-T. Wang, and X.-P. Wang, *Physical Review D* **107**, 095016 (2023).
  - [10] C.-T. Lu, *Phys. Rev. D* **108**, 115029 (2023), arXiv:2210.15648 [hep-ph].
  - [11] L. Calibbi, Z. Huang, S. Qin, Y. Yang, and X. Yin, *Physical Review D* **108**, 015002 (2023).
  - [12] C.-T. Lu, X. Luo, and X. Wei, *Chinese Physics C* **47**, 103102 (2023).
  - [13] K. Cheung and C. Ouseph, *Physical Review D* **108**, 035003 (2023).
  - [14] A. Alves, A. G. Dias, E. d. S. Almeida, and D. S. V. Gonçalves, *Physical Review D* **109**, 055013 (2024), arXiv:2306.14957 [hep-ph].
  - [15] S. Blasi, F. Maltoni, A. Mariotti, K. Mimasu, D. Paganani, and S. Tentori, “Top-philic ALP phenomenology at the LHC: the elusive mass-window,” (2024), arXiv:2311.16048 [hep-ph].
  - [16] C.-X. Yue, H. Wang, and Y.-Q. Wang, *Phys. Lett. B* **848**, 138368 (2024), arXiv:2311.16768 [hep-ph].
  - [17] C.-X. Yue, X.-Y. Li, and X.-C. Sun, *The European Physical Journal C* **84**, 1033 (2024), arXiv:2404.13226 [hep-ph].
  - [18] T. Li, Z. Qian, M. A. Schmidt, and M. Yuan, *Journal of*

- High Energy Physics **2024**, 232 (2024).
- [19] K. Cheung, C.-T. Lu, C. J. Ouseph, and P. Sarmah, “Exploring interference effects between two ALP effective operators at the LHC,” (2024), arXiv:2404.14833 [hep-ph].
- [20] Y. Hosseini and M. M. Najafabadi, Physical Review D **110**, 055026 (2024), arXiv:2408.11588 [hep-ph].
- [21] Z. Ding, Y.-n. Mao, and K. Wang, Journal of High Energy Physics **2025**, 87 (2025).
- [22] K. Cheung, C. J. Ouseph, and S. K. Kang, JHEP **04**, 024 (2025), arXiv:2412.08212 [hep-ph].
- [23] J. Sun, Z.-P. Xing, and S. Yun, Chin. Phys. **49**, 113109 (2025), arXiv:2501.15250 [hep-ph].
- [24] M. Tamaro and J. Zupan, “Axion searches at colliders,” (2025), arXiv:2505.00124 [hep-ph].
- [25] S. Bhattacharya, S. Jahedi, S. K. Manna, and A. Sil, (2025), arXiv:2505.00478 [hep-ph].
- [26] S.-s. Bao, Y. Ma, Y. Wu, K. Xie, and H. Zhang, Journal of High Energy Physics **2025**, 122 (2025), arXiv:2505.10023 [hep-ph].
- [27] S. Barbosa, M. Coelho, S. Fichet, G. G. d. Silveira, and M. Machado, Physical Review Letters **135**, 181801 (2025), arXiv:2506.10066 [hep-ph].
- [28] I. Brivio, M. B. Gavela, L. Merlo, K. Mimasu, J. M. No, R. d. Rey, and V. Sanz, The European Physical Journal C **77**, 572 (2017), arXiv:1701.05379 [hep-ph].
- [29] H. Georgi, D. B. Kaplan, and L. Randall, Physics Letters B **169**, 73 (1986).
- [30] J. Ren, D. Wang, L. Wu, J. M. Yang, and M. Zhang, Journal of High Energy Physics **2021**, 138 (2021), arXiv:2106.07018 [hep-ph].
- [31] L. Calibbi, T. Li, L. Mukherjee, and Y. Yang, Phys. Rev. D **110**, 115009 (2024), arXiv:2406.13234 [hep-ph].
- [32] K. Cheung, W. Hsiao, C. J. Ouseph, and C. Wang, “Probing the Gauge-boson Couplings of Axion-like Particle at the LHC and High-Luminosity LHC,” (2024), arXiv:2402.10550 [hep-ph].
- [33] A. Anuar, A. Biekötter, T. Biekötter, A. Grohsjean, S. Heinemeyer, L. Jappe, C. Schwanenberger, and G. Weiglein, Journal of High Energy Physics **2024**, 197 (2024), arXiv:2404.19014 [hep-ph].
- [34] B. Batell, H. Davoudiasl, R. Marcarelli, E. T. Neil, and S. Trojanowski, Phys. Rev. D **110**, 075039 (2024), arXiv:2407.15942 [hep-ph].
- [35] G. Haghghat and M. Mohammadi Najafabadi, Nucl. Phys. B **980**, 115827 (2022), arXiv:2106.00505 [hep-ph].
- [36] C. Han, M. L. López-Ibáñez, A. Melis, Ó. Vives, and J. M. Yang, JHEP **08**, 306 (2022), arXiv:2203.16376 [hep-ph].
- [37] Z.-M. Huang, C. Li, and Z. Liu, “Refined Low-Energy Supernova Constraints on Lepton Flavor Violating Axions,” (2025), arXiv:2510.22523 [hep-ph].
- [38] Y. Li and Z. Liu, “Supernova constraints on lepton flavor violating ALPs,” (2026), arXiv:2501.12075 [hep-ph].
- [39] L. Calibbi, D. Redigolo, R. Ziegler, and J. Zupan, Journal of High Energy Physics **2021**, 173 (2021), arXiv:2006.04795 [hep-ph].
- [40] J. L. Feng, T. Moroi, H. Murayama, and E. Schnapka, Physical Review D **57**, 5875 (1998), arXiv:hep-ph/9709411.
- [41] A.-Y. Bai, Y. Chen, Y. Chen, R.-R. Fan, Z. Hou, H.-T. Jing, H.-B. Li, Y. Li, H. Miao, H. Peng, A. A. Petrov, Y.-P. Song, J. Tang, J.-Y. Tang, N. Vassilopoulos, S. Vihonen, C. Wu, T.-Y. Xing, Y. Xu, Y. Yuan, Y. Zhang, G. Zhao, S.-H. Zhao, and L. Zhou, “Snowmass2021 Whitepaper: Muonium to antimuonium conversion,” (2022), arXiv:2203.11406 [hep-ph].
- [42] C. Degrande, C. Duhr, B. Fuks, D. Grellscheid, O. Mattelaer, and T. Reiter, Comput. Phys. Commun. **183**, 1201 (2012), arXiv:1108.2040 [hep-ph].
- [43] A. Alloul, N. D. Christensen, C. Degrande, C. Duhr, and B. Fuks, Comput. Phys. Commun. **185**, 2250 (2014), arXiv:1310.1921 [hep-ph].
- [44] J. Alwall, M. Herquet, F. Maltoni, O. Mattelaer, and T. Stelzer, Journal of High Energy Physics **2011**, 128 (2011), arXiv:1106.0522 [hep-ph].
- [45] F. Maltoni and T. Stelzer, Journal of High Energy Physics **2003**, 027 (2003).
- [46] G. D. V. Garcia, F. Kahlhoefer, M. Ovchinnikov, and A. Zaporozhchenko, Physical Review D **109**, 055042 (2024), arXiv:2310.03524 [hep-ph].
- [47] C. Bierlich *et al.*, SciPost Phys. Codeb. **2022**, 8 (2022), arXiv:2203.11601 [hep-ph].
- [48] J. d. Favereau, C. Delaere, P. Demin, A. Giammanco, V. Lemaître, A. Mertens, and M. Selvaggi, Journal of High Energy Physics **2014**, 57 (2014), arXiv:1307.6346 [hep-ex].
- [49] A. Collaboration, Physical Review D **98**, 092008 (2018), arXiv:1807.06573 [hep-ex].
- [50] L. Willmann, P. V. Schmidt, H. P. Wirtz, R. Abela, V. Baranov, J. Bagaturia, W. Bertl, R. Engfer, A. Großmann, V. W. Hughes, K. Jungmann, V. Karpuchin, I. Kisel, A. Korenchenko, S. Korenchenko, N. Kravchuk, N. Kuchinsky, A. Leuschner, V. Meyer, J. Merkel, A. Moiseenko, D. Mzavia, G. Zu Putlitz, W. Reichart, I. Reinhard, D. Renker, T. Sakhelashvilli, K. Träger, and H. K. Walter, Physical Review Letters **82**, 49 (1999).